Applied Ocean Research 119 (2022) 102934

Contents lists available at ScienceDirect

Applied Ocean Research

journal homepage: www.elsevier.com/locate/apor

An upright bottomless vertical cylinder with baffles floating in waves

Maël Moreau [a,*], Trygve Kristiansen [a], Babak Ommani [b], Bernard Molin [a,c]

[a] Norwegian University of Science and Technology (NTNU), Trondheim NO-7491, Norway
[b] SINTEF Ocean, 7450 Trondheim, Norway
[c] Aix-Marseille Université, CNRS, Centrale Marseille, IRPHE, Marseille 13013, France

ARTICLE INFO

Keywords:
Potential flow theory
Diffraction and radiation problems
Sloshing
Model tests

ABSTRACT

Damping of the surge and pitch motions, as well as the first lateral sloshing mode in a rigid free-floating upright circular dock with bilge boxes and open bottom is investigated. Model tests are carried out on a 0.80 m diameter model in regular waves with wave periods near the highest natural sloshing period, and the internal free-surface elevation and model's rigid body motions are measured. Perforated and solid annular baffles of relatively small widths are also installed inside the dock at various submergences. The experimental results are compared to a semi-analytical approach, where a three-dimensional domain decomposition method based on linear potential flow theory is adopted to calculate the hydrodynamic coefficients and exciting forces in heave, surge and pitch. A reduced natural sloshing frequency, as well as a damping ratio estimated from the energy dissipated due to flow separation from the baffles, are introduced in the free-surface boundary conditions to model the effects of the baffle. It shows good agreement with experimental data when the ratio between the draft of the baffle and the internal radius of the cylinder is $d_B/a = 0.27$, and tends to under-predict the damping ratio for shallower drafts, most likely due to free-surface interactions. The solid baffle damps the sloshing response most efficiently, reducing the amplitude at the resonant peak by more than 56%.

1. Introduction

This study aims to investigate the rigid-body motions of a free-floating bottomless upright circular cylinder with bilge boxes, also referred to as a dock, in regular waves. The dock was suggested for the assembly of SPAR-type floating offshore wind turbines (FOWT) directly on site, the walls of the cylinder acting as protecting shields against external waves. The sloshing resonance becomes a critical issue at typical operational weather conditions. The heave, pitch, and piston mode resonance can be moved to higher periods thanks to design optimisations, as showed by Jiang et al. (2020). However, it is not the case for the first transverse sloshing mode, which is the main focus of this paper. Special attention is made to damping introduced by annular baffles mounted to the interior walls of the dock.

The radiation and diffraction problems are solved in the frequency domain, under the classical linear potential flow assumptions. A domain-decomposition approach using matched eigenfunction expansions is adopted, with the advantage of being fast and economical. Such analytical methods were extensively treated in the literature, both for two-dimensional (2D) and three-dimensional (3D) geometries. Miles and Gilbert (1968), later completed by Garrett (1971), solved the scattering problem of a closed-bottom circular cylinder in finite water depth. Yeung (1980) and Sabuncu and Calisal (1981) solved the radiation problem for the same geometry. The case of a bottomless circular cylinder with finite wall thickness was considered by Mavrakos (1988, 1985), and is extended here to include bilge boxes at the bottom.

Annular baffles installed on the cylinder's internal wall, below the free surface, to damp the first transverse sloshing mode, are the centre of attention. Experimental campaigns in cylindrical tanks (Abramson, 1966) pointed out the superior efficiency of baffles over other types of damping devices. Isaacson and Premasiri (2001) estimated the equivalent linear damping of a baffle in a rectangular tank from the dissipation of energy over one period of oscillation, caused by the flow separation at the sharp edge. The baffle is reduced to a flat plate, and Morison formula (Morison et al., 1950) is used to calculate the viscous work. Faltinsen and Timokha (2009) introduced such linear damping ratios in the free-surface boundary condition. Furthermore, they showed how to estimate shifted natural sloshing frequencies due to the presence of a small internal body in a tank based on variational formulations, which can be expressed as function of its added mass. A simple case is flat plates, for which the hydrodynamic coefficients have been well-studied (Graham, 1980). Graham (1980) presented explicit expressions of the inertial and drag coefficients for oscillatory flows around bodies with sharp corners, valid for low Keulegan–Carpenter (KC) numbers,

* Corresponding author.
E-mail address: mael.k.i.moreau@ntnu.no (M. Moreau).

https://doi.org/10.1016/j.apor.2021.102934
Received 30 March 2021; Received in revised form 18 October 2021; Accepted 20 October 2021
Available online 7 January 2022

typically KC<2, and provided empirical coefficients for simple geometries. Mentzoni (2020) used the same relations for perforated plates with good results, determining the empirical coefficients through numerous CFD simulations. In the present work we investigate both solid and perforated baffles, at different submergences.

Potential flow boundary-value problems in a closed-bottom cylinder with annular baffles were solved by Gavrilyuk et al. (2006), or by Wang et al. (2016) for multiple baffles. The latest study set the same domain decomposition approach used in this work for the open-bottom dock without baffle. One interesting observation pointed out in their studies is the dependency of the natural surface modes on the location of the baffle, in particular on the radial surface profiles (Wang et al., 2016). We do not account for this local disturbance, something that might be non-negligible and could be studied in future work.

Baffles are a quite efficient mean of damping the sloshing response, and therefore the coupled surge-pitch and resonant sloshing inside the dock. Without baffles, the resonant free-surface responses are 3–4 times higher than the incident waves. The surge and pitch motions of the dock are also considerable due to the sloshing-induced loads. Damping is therefore necessary for the dock to satisfy the criteria of small relative vertical and horizontal motions between the cranes and the wind turbine when installing the different components, from the tower to the blades. The present paper treats the open dock without the presence of a FOWT, and represents a first step toward a future fully coupled model including the SPAR of a FOWT. Emphasis is made on an efficient model, including the damping effect of the baffles based on physical reasoning. There are several ways to do this, and we have chosen the following strategy. Our model has two main steps. In the first step, the rigid-body motions of the dock, without baffles, are solved by means of a matched eigenfunction expansion, similar to Mavrakos (1988, 1985), but extended to include the bilge boxes. Next, we study the interior domain separately in terms of the linear modal analysis developed by Faltinsen and Timokha (2009), i.e. as if it was a closed tank with bottom. This is justified by the fact that the draft of the dock is in the same order as the inner diameter, and we can therefore neglect the water motions near the bottom when studying the first sloshing mode. The benefit with the modal analysis is that damping can easily be included by a damping term in the modal equations. The damping of the baffles is quadratic in nature and included by means of equivalent linearisation. We apply the 2D Morison equation on an angular section of the dock with KC number dependent drag coefficients, and integrate around the dock. Further, the baffles change the natural period. This is accounted for by using variational statements, also found in Faltinsen and Timokha (2009). Iteration is applied to reach a reduced sloshing amplitude. The loads on the interior walls, as predicted in the first step is now replaced by the loads predicted in the second step, in terms of interior added mass and damping coefficients. The number of iterations needed is modest, typically between 5 and 15, and the model is robust and fast.

The paper is organised as follows. In Section 2, the diffraction and radiation problems are solved in surge, pitch and heave for the dock without baffle. In Section 3, a convergence study is made on the number of eigenmodes required in the analytical method presented in Section 2. Added masses and damping coefficients, as well as exciting forces are compared to the ones obtained with the commercial potential code WAMIT (Lee and Newman, 2006). In Section 4, the effects of the annular baffles on sloshing are first studied in closed-bottom circular cylinder, and in tank-fixed coordinate system, before deriving the equation of motions in an Earth-fixed referential for the real geometry. Model tests are presented in Section 5, and the results discussed in Section 6.

2. Theoretical description

We first neglect the effect of flow separation and work under the assumption of potential flow theory. Further, we use the wave slope to linearise the boundary value problem at hand. The diffraction and radiation problems associated with the geometry presented in Fig. 1 are solved using a domain-decomposition (DD) approach, for incident waves propagating along the positive x-axis. The domain Ω is divided into four subdomains, denoted I, II, III and IV. The body's mean wetted surface is denoted S_0. Complex notations are used to simplify the calculations, where the physical quantities correspond to the real parts of the given variables.

2.1. Diffraction problem

Regular linear waves of amplitude A and frequency ω are scattered by the fixed structure. The velocity potential of the incident waves is given by Eq. (1) using cylindrical coordinates:

$$\boldsymbol{\Phi}_I = -i\frac{Ag\cosh(k(z+h))}{\omega\cosh(kh)}e^{i(kr\cos(\theta)-\omega t)}. \tag{1}$$

$g = 9.81$ m/s is the gravitational acceleration, and k the wave number, coupled with ω by the linear dispersion relationship $\omega^2 = gk\tanh(kh)$. The complex exponential is then decomposed in Fourier series, and the total scattered potential $\boldsymbol{\Phi}_S$, summations of the incident and diffracted flows, can be expressed under the same form:

$$\boldsymbol{\Phi}_I = -i\frac{gA}{\omega}\frac{\cosh(k(z+h))}{\cosh(kh)}\sum_{p=0}^{\infty}\epsilon_p i^p J_p(kr)\cos(p\theta)e^{-i\omega t}, \tag{2}$$

$$\boldsymbol{\Phi}_S = -i\omega A\sum_{p=0}^{\infty}\epsilon_p i^p \phi_p(r,z)\cos(p\theta)e^{-i\omega t}, \tag{3}$$

where $J_p,\ p\in\mathbb{N}$ is the Bessel function of the first kind and p_{th} order, i the imaginary unit, $\epsilon_p,\ p\in\mathbb{N}$ the Neumann's notation

$$\begin{cases}\epsilon_0 = 1\\ \epsilon_p = 2,\ p\in\mathbb{N}^*,\end{cases} \tag{4}$$

and where $\mathbb{N}^* = \mathbb{N}\backslash\{0\}$. The modal potentials $\phi_p,\ p\in\mathbb{N}$ are solved independently, due to the orthogonality of the cosine function that we exploit in the matching of pressure and normal velocities later on. They satisfy the Laplace Eq. (5) and the conditions (6), (7) and (8) on the boundaries of Ω:

$$\frac{\partial^2\phi}{\partial z^2} + \frac{1}{r}\frac{\partial}{\partial r}\left(r\frac{\partial\phi}{\partial r}\right) - \frac{p^2}{r^2}\phi = 0 \ \text{ in } \Omega, \tag{5}$$

$$\frac{\partial\phi}{\partial z} = \frac{\omega^2}{g}\phi \ \text{ on } z = 0, \tag{6}$$

$$\frac{\partial\phi}{\partial z} = 0 \ \text{ on } z = -h, \tag{7}$$

$$\frac{\partial\phi}{\partial n} = 0 \ \text{ on } S_0. \tag{8}$$

In addition, outgoing diffracted waves should vanish far from the body, this radiation condition can be expressed (Sommerfeld, 1948): $\lim_{r\to\infty}\sqrt{kr}\left(\frac{\partial(\boldsymbol{\Phi}_S-\boldsymbol{\Phi}_I)}{\partial r} - ik(\boldsymbol{\Phi}_S-\boldsymbol{\Phi}_I)\right) = 0$. The free-surface elevation is then obtained from the linearised kinematic free-surface boundary condition, i.e. $\frac{\partial\zeta}{\partial t} = \frac{\partial\boldsymbol{\Phi}_S}{\partial z}$.

The dispersion relationship

$$\frac{\omega^2}{g} + \alpha_q\tan(\alpha_q h) = 0 \tag{9}$$

is solved in domains I and IV (cf. Fig. 1), $\alpha_q,\ q\in\mathbb{N}^*$ are the real solutions by increasing order of Eq. (9), and $\alpha_0 = -ik$. Similar relations hold in domain III, above the bilge boxes, for the local water depth d. $\beta_q,\ q\in\mathbb{N}^*$ are the real solutions of

$$\frac{\omega^2}{g} + \beta_q\tan(\beta_q d) = 0, \tag{10}$$

where $\beta_0 = -i\tilde{k}$, and $\tilde{k}$ is the wave number in domain III for the water depth d.

The set of orthonormal functions

$$Z_q(z) = N_q^{-\frac{1}{2}}\cos(\alpha_q(z+h)),\ q\in\mathbb{N} \tag{11}$$

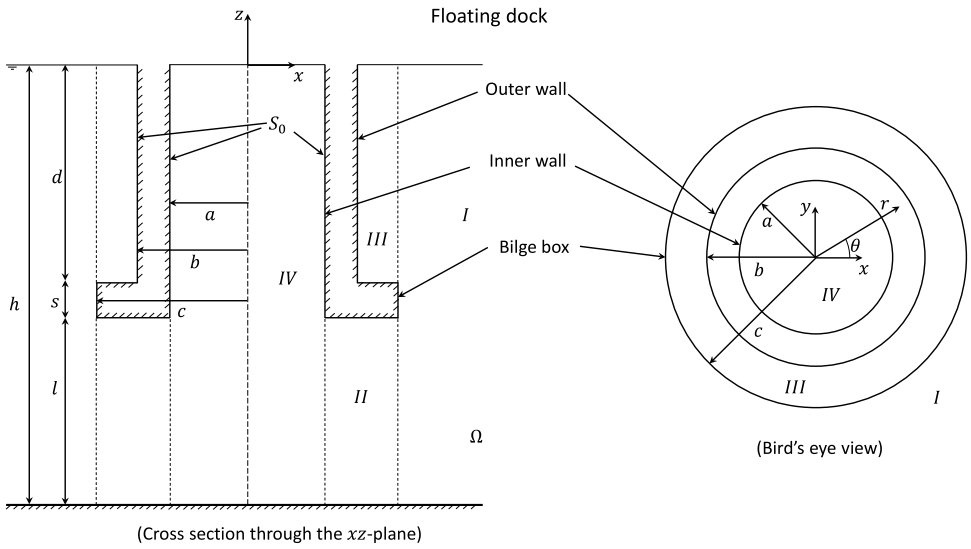

Fig. 1. Sketch of the upright, circular, bottomless floating dock with bilge boxes. Explanation of parameters and the division of the domain Ω into the four subdomains denoted I–IV used for the present analysis. A Cartesian Earth-fixed coordinate system $Oxyz$ is adopted with the origin at the mean free-surface and the z-axis positive upwards.

are introduced, solutions in z of the Laplace equation in domains I and IV. N_q, $q \in \mathbb{N}$ are normalised coefficients, assuring the orthonormality condition (explicit expressions of N_q are given in the online supplement). Similar functions are defined for the domain III:

$$\tilde{Z}_q(z) = \tilde{N}_q^{-\frac{1}{2}} \cos(\beta_q(z+d)), \quad q \in \mathbb{N}. \tag{12}$$

2.1.1. Potential expansions

The potential ϕ_p are determined by separation of variables as the summation of the solutions of the Laplace equation,

$$\phi_p^I(r,z) = \left[J_p(kr) - \frac{J_p(kc)}{H_p(kc)} H_p(kr)\right] \frac{Z_0(z)}{Z_0'(0)} + b\sum_{q=0}^{\infty} A_{p,q}^I \frac{K_p(\alpha_q r)}{K_p(\alpha_q c)} Z_q(z), \tag{13}$$

$$\phi_p^{II}(r,z) = b\sum_{q=0}^{\infty} \epsilon_q [A_{1,p,q}^{II} P_{p,q}^{II}(r) + A_{2,p,q}^{II} Q_{p,q}^{II}(r)] \cos\left(\frac{q\pi(z+h)}{l}\right), \tag{14}$$

$$\phi_p^{III}(r,z) = b\sum_{q=0}^{\infty} [A_{1,p,q}^{III} P_{p,q}^{III}(r) + A_{2,p,q}^{III} Q_{p,q}^{III}(r)] \tilde{Z}_q(z), \tag{15}$$

$$\phi_p^{IV}(r,z) = b\sum_{q=0}^{\infty} A_{p,q}^{IV} \frac{I_p(\alpha_q r)}{I_p(\alpha_q a)} Z_q(z). \tag{16}$$

In domain I, it includes the contribution of the incident waves (Garrett, 1971), cf. Eq. (13), where I_p and K_p are the modified Bessel functions H_p is the Hankel function of the first kind, and we have the relationship $K_p(-ikr) = \frac{1}{2}\pi i^{p+1} H_p(kr)$ and $I_p(\alpha_0 r) = J_p(kr)$. The eigen-modes are multiplied by the external radius b to keep the unknowns $A_{p,q}^I$ non-dimensional. The expansions of the pth potential mode in the domains II and III are given by Eqs (14) and (15), where the functions $P_{p,q}(r)$ and $Q_{p,q}(r)$ have been defined similar to Mavrakos (1985) in order to simplify the matching conditions for the potential at the boundaries with adjacent domains, and to lighten the notations (their explicit expressions are given in the online supplement). Finally, the potential expansions in the domain IV are given by (16).

2.1.2. Matching

For each mode $p \in \mathbb{N}$, we have introduced an infinite number of unknowns $A_{p,q}$, $q \in \mathbb{N}$, which remain to be determined by establishing the matching conditions on all the vertical boundaries.

First, the continuity of the dynamic pressure between two consecutive domains is enforced over the corresponding boundary, in the way of Garrett (1971):

$$\int_{-h}^{-(d+s)} \phi_p^{II}(a,z) \cos\left(\frac{q\pi(z+h)}{l}\right) dz = \int_{-h}^{-(d+s)} \phi_p^{IV}(a,z) \cos\left(\frac{q\pi(z+h)}{l}\right) dz, \tag{17}$$

$$\int_{-h}^{-(d+s)} \phi_p^{II}(c,z) \cos\left(\frac{q\pi(z+h)}{l}\right) dz = \int_{-h}^{-(d+s)} \phi_p^{I}(c,z) \cos\left(\frac{q\pi(z+h)}{l}\right) dz, \tag{18}$$

$$\int_{-d}^{0} \phi_p^{III}(c,z) \tilde{Z}_q(z) dz = \int_{-d}^{0} \phi_p^{I}(c,z) \tilde{Z}_q(z) dz. \tag{19}$$

Then the continuity of the normal velocity, as well as the non-penetration condition on the vertical walls are assured by integration over the whole water depth,

$$\int_{-d}^{0} \frac{\partial \phi_p^{III}}{\partial r}(b,z) \tilde{Z}_q(z) dz = 0, \tag{20}$$

$$\int_{-h}^{0} \frac{\partial \phi_p^{I}}{\partial r}(c,z) Z_q(z) dz = \int_{-h}^{-(d+s)} \frac{\partial \phi_p^{II}}{\partial r}(c,z) Z_q(z) dz + \int_{-d}^{0} \frac{\partial \phi_p^{III}}{\partial r}(c,z) Z_q(z) dz, \tag{21}$$

$$\int_{-h}^{0} \frac{\partial \phi_p^{IV}}{\partial r}(a,z) Z_q(z) dz = \int_{-h}^{-(d+s)} \frac{\partial \phi_p^{II}}{\partial r}(a,z) Z_q(z) dz. \tag{22}$$

Because of the orthogonality properties of the functions Z_q, $\tilde{Z}_q$, and cos, respectively, these equations result in a linear system for the coefficients $A_{p,q}$, $q \in \mathbb{N}$, independently for each $p \in \mathbb{N}$. In practice, the sums from the potential expansions must be truncated. We write N_S the total number of potentials describing the diffracted flow in Eq. (3), and N_I, N_{II}, N_{III} and N_{IV} the numbers of modes kept in the domains I, II, III and IV, i.e. in the expansions (13), (14), (15) and (16) for the potential ϕ_p. The same number of modes in the domains I to IV are chosen for each $p \in [0, N_S]$ for the sake of simplicity.

Eqs. (17) to (20) give a relationship between each unknown coefficients A^{II} and A^{III} as a function of the coefficients A^I and A^{IV}, which can be substituted in the right hand side of Eqs (21) and (22). The order of the linear systems resulting from the matching conditions is then reduced to $N_I + N_{IV}$ for all fixed $p \in [0, N_S]$. This system is condensed by the matricial equation

$$\boldsymbol{A}^S = \mathbb{B}^S \boldsymbol{A}^S + \boldsymbol{C}^S \tag{23}$$

for the variable $\boldsymbol{A}^S = \left[A_{p,1}^I \cdots A_{p,N_I}^I A_{p,1}^{IV} \cdots A_{p,N_{IV}}^{IV}\right]^T$. The upper index S stands here for "Scattering". The coefficients of the matrices $\mathbb{B}^S$, $\boldsymbol{C}^S$ and the relation to the remaining coefficients $A_{p,q}$ are given in the online supplement.

2.1.3. Exciting forces and moment

The hydrodynamic exciting forces and moments are derived by integrating the dynamic pressure on the walls of the structure:

$$F_j^S = \rho \int\int_{S_0} \frac{\partial \Phi_S}{\partial t} n_j dS = -\omega^2 A \rho \sum_{p=0}^{\infty} \epsilon_p i^p \times \left[\int\int_{S_0} \phi_p(r,z) \cos(p\theta)\, n_j dS \right] e^{-i\omega t} \quad j \in [1,6]. \tag{24}$$

$\boldsymbol{n} = [n_1\ n_2\ n_3]^T$ is the unit vector pointing outward the body, $\boldsymbol{r} = [r\cos(\theta)\ r\sin(\theta)\ z]^T$ is the position vector, and $[n_4\ n_5\ n_6]^T = \boldsymbol{r} \times \boldsymbol{n}$. ρ is the water density. Their analytical expressions are given in the online supplement.

2.2. Radiation problem

Due to symmetry of the body geometry, and mooring, we only consider surge, heave and pitch motions, respectively denoted $\eta_j = \overline{\eta}_j e^{-i\omega t}$, $j \in [1,3,5]$. The forced pitch motion is defined about the Oy axis (cf. Fig. 1). $\overline{\eta}_j$ is the complex amplitude. $\dot{\eta}$ is the body's velocity for each of the three degrees of freedom (DoFs). In the framework of linear potential flow theory, the response of the fluid can be expressed by

$$\Phi_R(r,\theta,z,t) = \phi(r,z)\dot{\eta}\cos(p\theta), \tag{25}$$

$p = 0$ corresponds to the symmetric DoF, heave, and $p = 1$ to the anti-symmetric DoFs, surge and pitch. The potentials ϕ satisfy the Laplace Eq. (5), the free-surface and bottom-boundary conditions (6) (7), the body-boundary condition $\frac{\partial \phi}{\partial n} = n_j$, $j = 1$, 3 and 5 for each DoF respectively, as well as the radiation condition for outgoing radiated waves $\lim_{r\to\infty} \sqrt{kr}(\frac{\partial \phi}{\partial r} - ik\phi) = 0$.

2.2.1. Potential expansions

The potentials in the domains I and IV correspond to the symmetric and anti-symmetric modes of the diffraction problem, with the difference that there is no incident waves and all the radiated potentials have to vanish for large r in domain I. They are given by

$$\phi^I(r,z) = \psi \sum_{q=0}^{\infty} A_q^I \frac{K_p(\alpha_q r)}{K_p(\alpha_q c)} Z_q(z), \tag{26}$$

$$\phi^{IV}(r,z) = \psi \sum_{q=0}^{\infty} A_q^{IV} \frac{I_p(\alpha_q r)}{I_p(\alpha_q a)} Z_q(z), \tag{27}$$

where $\psi = b$ for the problems in heave and surge, and $\psi = b^2$ for the problem in pitch.

The expansions are chosen to satisfy exactly all the horizontal boundary conditions in their corresponding domain. In the domains II and III, where a horizontal body-boundary condition is present, and similar to Yeung (1980), the potential is decomposed in:

- A particular solution ϕ_m that satisfies the Laplace equation, and all the horizontal boundary conditions when the forced motion is applied, but without any condition on the vertical boundaries (taken care of by ϕ_h).
- A homogeneous solution ϕ_h that satisfies the Laplace equation when the structure is fixed, and which assures that the vertical matching with adjacent domains or body-boundary conditions are satisfied.

The potentials in the domain II and III are thus expressed as $\phi^{II} = \phi_h^{II} + \phi_m^{II}$ and $\phi^{III} = \phi_h^{III} + \phi_m^{III}$. The functions (28) to (31) are proposed for the particular solutions, and the homogeneous parts are given by (32) and (33):

$$\phi_m^{II} = \frac{(z+h)^2 - \frac{r^2}{2}}{2(h-(d+s))} \text{ in heave,} \tag{28}$$

$$\phi_m^{II} = -\frac{r(z+h)^2 - \frac{r^3}{4}}{2(h-(d+s))} \text{ in pitch,} \tag{29}$$

$$\phi_m^{III} = z + \frac{g}{\omega^2} \text{ in heave,} \tag{30}$$

$$\phi_m^{III} = -(z + \frac{g}{\omega^2})r \text{ in pitch,} \tag{31}$$

$$\phi_h^{II}(r,z) = \psi \sum_{q=0}^{\infty} \epsilon_q [A_{1,q}^{II} P_{m,q}^{II}(r) + A_{2,q}^{II} Q_{m,q}^{II}(r)] \cos\left(\frac{q\pi(z+h)}{l}\right), \tag{32}$$

$$\phi_h^{III}(r,z) = \psi \sum_{q=0}^{\infty} [A_{1,q}^{III} P_{m,q}^{III}(r) + A_{2,q}^{III} Q_{m,q}^{III}(r)] \bar{Z}_q(z). \tag{33}$$

We note that for the problem in surge, $\phi_m^{II} = \phi_m^{III} = 0$.

2.2.2. Matching

As for the diffraction problem, the continuity of the dynamic pressure between two domains is assured by integration over the domains' common boundary, while the conditions on the normal velocity for the problems in surge, heave, and pitch, respectively, are imposed over the whole water depth.

The sums are once again truncated, and the modes kept in the four domain for each DoF denoted N_I, N_{II}, N_{III} and N_{IV}. Similar to the diffraction problem, the matching equations are expressed by the matrical equation

$$\boldsymbol{A}^R = \mathbb{B}^R \boldsymbol{A}^R + \boldsymbol{C}^R \tag{34}$$

of order $N_I + N_{IV}$ for each DoF, and for the variable $\boldsymbol{A}^R = \left[A_1^I \cdots A_q^I\ A_1^{IV} \cdots A_q^{IV}\right]^T$. The analytical expressions of these matrices, and the relation to the remaining coefficient A_q are given in the online supplement.

2.2.3. Added mass and damping coefficients

Once the potential is known in each domain, the hydrodynamic coefficients can be determined (Newman, 1977) by

$$\begin{cases} a_{i,j} = -\rho\, \mathrm{Re}\left[\int\int_{S_0} \phi_j \cos(p\theta) n_i dS\right] \\ b_{i,j} = -\rho\omega\, \mathrm{Im}\left[\int\int_{S_0} \phi_j \cos(p\theta) n_i dS\right] \end{cases} (i,j) \in \{1,3,5\}^2. \tag{35}$$

By symmetry, when there is no current or forward speed, $a_{1,5} = a_{5,1}$ and $b_{1,5} = b_{5,1}$, and all the coefficient expressing a coupling between heave and either surge or pitch are null.

The analytical expressions of these coefficients are given in the online supplement.

3. Verification of the potential code

Our theory is compared with the commercial Boundary Element Method (BEM) software WAMIT (Lee and Newman, 2006) to investigate the convergence of the results. The results of these convergence studies are presented in Figs. 2 and 3 for $a/b = 0.75$, $c/b = 1.22$, $s/b = 0.13$, $(d+s)/b = 2$ and $h/b = 5$.

As illustrated in Figs. 2 and 3, the convergence for the radiation problem in surge is reached for only 10 modes in each domain, and the radiation problem in pitch for 50 modes in each domain. In forced heave, a higher number of modes in the domain I relative to the domains II and III is required to represent the flow in the vicinity of the bilge boxes at the bottom of the dock. It is chosen to use $N_I = 100$, $N_{II} = N_{III} = 20$ and $N_{IV} = 50$ for all simulations. The convergence of the exciting force in heave, particularly its phase, is very numerically sensitive, due to that the waves are short compared to the dock's draft, and the pressures are very small at the bottom of the dock. In addition, a study carried out for the free-surface elevation and the dynamic pressure field at several locations showed that $N_S = 12$ was a reasonable number of modes to achieve convergence in Eq. (3), while $N_S = 2$ provides the desired forces and moments from the diffraction problem. This latter number will be retained, since the incident waves

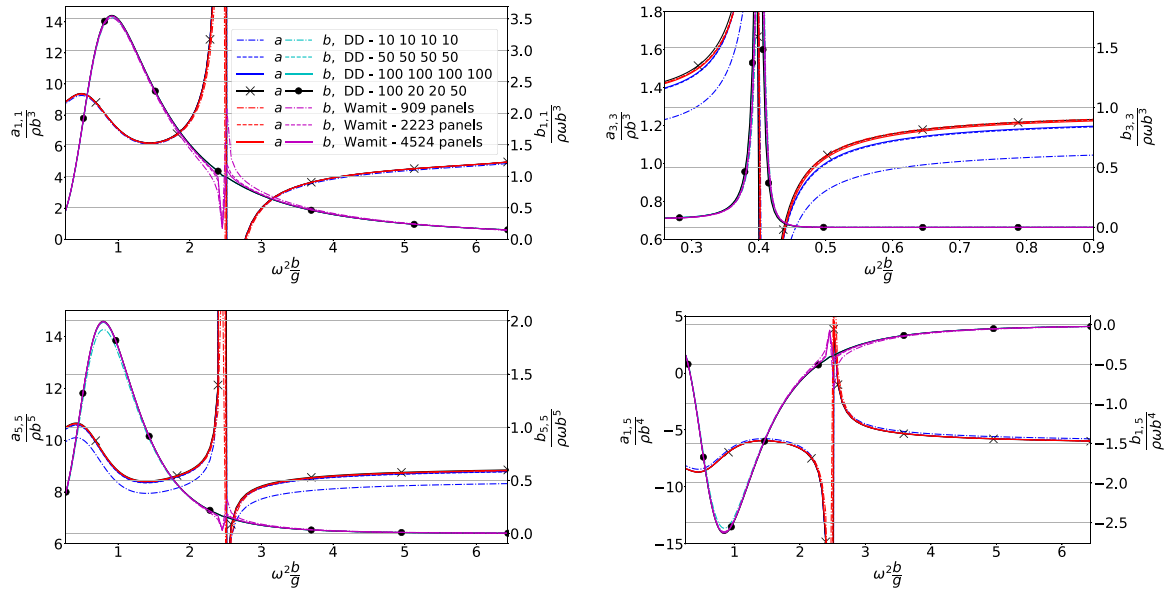

Fig. 2. Non-dimensional added mass (left axis) and damping coefficients (right axis) computed by the present DD method and the panel code WAMIT. Surge in the top left corner, heave in the top right corner, pitch in the bottom left corner, and coupled coefficients in surge and pitch in the bottom right corner. In the legend, a and b stand for the added mass and damping coefficients, respectively, and the number of modes associated to the domain decomposition (DD) method are given in the order from N_I to N_{IV}.

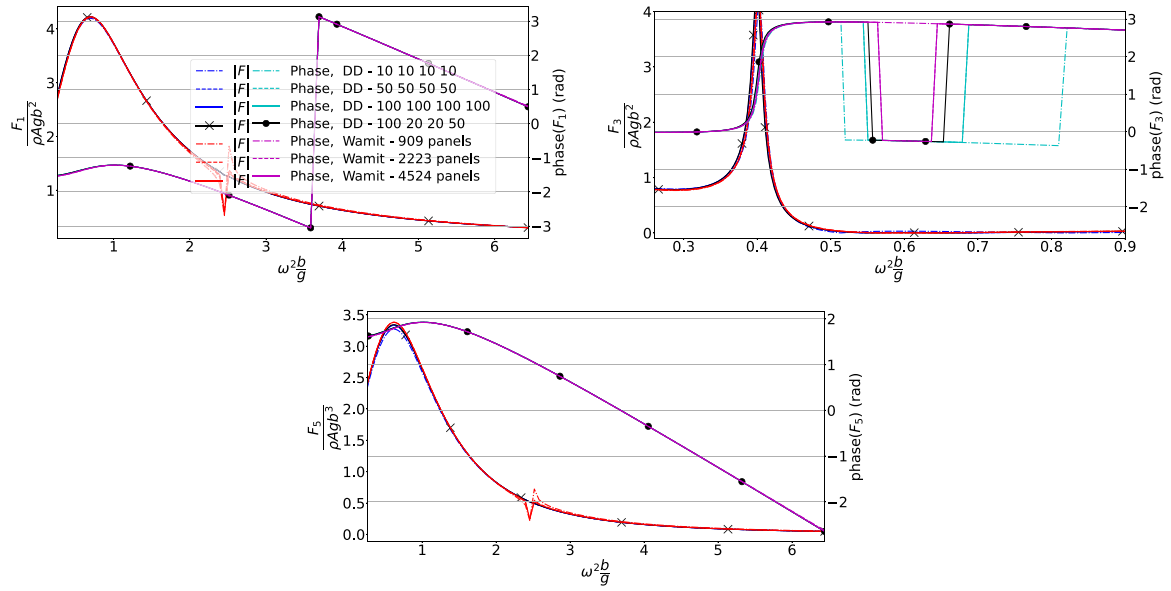

Fig. 3. Non-dimensional amplitude of exciting forces and moments (left axis) and their phases (right axis) computed by the present DD method and the panel code WAMIT. Surge in the top left corner, heave in the top right corner, and pitch in the bottom. The same number of modes are tested as in Fig. 2.

are too small to cause any perturbation of the free surface inside the dock when this one is fixed.

The peak at $\omega^2 b/g = 0.40$ observed from the problems in heave (cf. upper right figure in Fig. 2) corresponds to the piston-mode frequency described by Molin (2001). The second peak at $\omega^2 b/g = 2.45$ observed for the added mass in surge and pitch, cf. Fig. 3, corresponds to the first lateral sloshing mode. Analytical formulas for cylinders with closed bottom (Faltinsen and Timokha, 2009) give a very good estimation of this natural frequency when the draft of the dock is large.

4. Modelling of the annular damping baffles based on linear modal sloshing theory

A thin annular baffle of width $a_B/a = 0.17$, submergence d_B and thickness $t/a = 0.017$ is installed on the internal wall of the dock, as in Fig. 4. The baffle is assumed to always remain fully submerged. In order to include it in our model without introducing any additional domains in the DD method, we use established solutions for sloshing inside closed-bottom upright circular tanks, referred to as linear modal theory (Faltinsen and Timokha, 2009). The dock is indeed designed such that the draft d fulfils $\lambda/d < 2$ near resonance of the first sloshing mode, λ being the wave length of the incident waves, and such that the natural periods in heave and pitch are higher than the considered wave periods. It results that the fluid motion at the bottom of the dock is negligible. For instance, the dynamic pressure calculated with the method presented above reaches less than 1% of its maximal value at the free surface, and is mainly caused by pitch motions. We note in particular that the diffraction problem is unchanged when the baffle is installed.

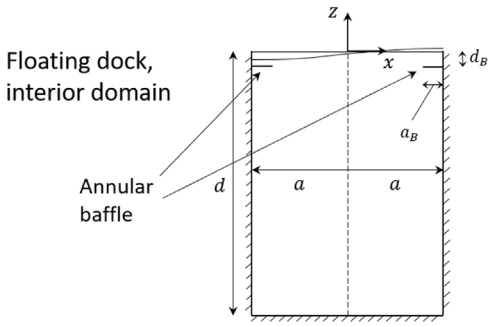

Fig. 4. Sketch of the centre-plane of the internal domain of the floating dock which is represented with a closed-bottom (closed) tank in our combined DD method to include the effect of baffles in the linear modal equations. The baffle draft d_B and width a_B are illustrated. The draft $d+s$ in Fig. 1 is re-written d in this section for lighter notations. $Oxyz$ is here a tank-fixed coordinate system.

The baffle introduces two main effects: a shift in the natural sloshing frequencies, as well as the desired damping. We consider that they affect only the first sloshing mode in the following analysis, as this is the one that is excited mainly, and it will therefore dominate the internal flow entirely.

4.1. Linear modal theory

The absolute potential $\Phi(x,y,z,t)$ inside a closed upright circular cylinder is given by Eq. (36), where Ω is the Stokes–Joukowski potential associated with pitch motion, cf. Eq. (38), φ_q the eigenfunctions determined from the spectral problem (Faltinsen and Timokha, 2009), cf. Eq. (37), and $R_q(t)$ unknown time-dependent coefficients:

$$\Phi(x,y,z,t) = \dot{\eta}_1 r\cos(\theta) + \dot{\eta}_5\Omega + \sum_{q=1}^{\infty} R_q(t)\varphi_q(r,\theta,z), \tag{36}$$

$$\varphi_q(r,\theta,z) = \frac{J_1\left(k_q r\right)}{J_1(k_q a)}\frac{\cosh\left(k_q(z+d)\right)}{\cosh\left(k_q d\right)}\cos(\theta), \tag{37}$$

$$\Omega(r,\theta,z) = \left[rz - 4a\sum_{p=1}^{\infty}\frac{J_1\left(k_p r\right)}{J_1\left(k_p a\right)k_p\left(k_p^2a^2-1\right)}\frac{\sinh(k_p(z+\frac{d}{2}))}{\cosh(k_p\frac{d}{2})}\right]\cos(\theta). \tag{38}$$

The potential Φ is caused by the surge and pitch motions of the dock. The first two terms of Eq. (36) describe the motion of the internal water volume with a rigid free surface when the cylinder is under forced motions, while the third term represents standing waves in the tank-fixed coordinate system.

The draft $d+s$ of the dock is re-written d in this section for lighter notations. Because the problem is anti-symmetric, only the eigenfunctions in $\cos(\theta)$ appear in Eq. (37). The wave numbers k_q are the roots by increasing order of $J_1'(k_q a) = 0$, and the corresponding natural frequencies obtained from the dispersion relationship:

$$\sigma_q = \sqrt{g k_q \tanh\left(k_q d\right)} = \sqrt{\kappa_q g}. \tag{39}$$

While the expansions from the DD method are chosen based on the exciting frequency ω of incident waves, the expansion in Eq. (36) is based on natural sloshing modes which only depend on the geometry of the structure.

The same eigen-functions are used to express the free-surface elevation relative to $z=0$:

$$\zeta(r,\theta,t) = \sum_{q=1}^{\infty}\beta_q(t)\varphi_q(r,\theta,0), \tag{40}$$

where $\beta_q(t)$ are unknown modal coefficients.

Making use of the orthogonality properties of the eigen-functions φ_q in r and θ, the modal Eqs. (41) and (42) for R_q and β_q are obtained by multiplying the kinematic and dynamic free-surface boundary conditions by $J_1\left(k_q r\right)$, $q\in\mathbb{N}^*$ and integrating over the water surface area Σ_0 in the cylinder:

$$\dot{\beta}_q = \kappa_q R_q, \tag{41}$$

$$\ddot{\beta}_q + 2\xi_q\sigma_q\dot{\beta}_q + \sigma_q^2\beta_q = K_q(t). \tag{42}$$

An equivalent linear damping term, expressed by the damping ratio ξ_q is added to include the viscous damping when a baffle is installed.

The excitation term of the sloshing $K_q(t) = -\omega^2\tilde{P}_{q,1}\overline{\eta}_1 e^{-i\omega t} - \omega^2\tilde{P}_{q,5}\overline{\eta}_5 e^{-i\omega t}$, is linearly dependent on the anti-symmetric rigid body motions. The coefficients $\tilde{P}_{q,1}$ and $\tilde{P}_{q,5}$ are given in the online supplement. The transient part of the solution vanishes exponentially in time at the rate $-\xi_q\sigma_q$, and only the forcing part remains, given for R_q by

$$R_q(t) = \frac{g}{\sigma_q^2}\frac{i\omega K_q(t)}{2i\omega\sigma_q\xi_q + \omega^2 - \sigma_q^2} = f_q(\omega)K_q(t). \tag{43}$$

4.2. Shifted sloshing frequency due to an annular baffle

The eigen-functions φ_q are assumed unchanged when the baffle is introduced, however the natural sloshing frequency σ_1 is shifted due to the added mass of the baffle. According to Faltinsen and Timokha (2009), this effect can be expressed as:

$$\frac{\sigma_1'^2}{\sigma_1^2} = 1 - \frac{\int_0^{2\pi}\left.\frac{\partial\varphi_1}{\partial z}\right|^2_{\substack{r=a\\ z=-d_B}} A^{plate}\mathrm{d}\theta}{\rho\kappa_1\int_{\Sigma_0}\varphi_1^2\mathrm{d}S}, \tag{44}$$

where A^{plate} is the two-dimensional added mass of a flat plate perpendicular to a wall. It is given analytically by Eq. (45) as half of the added mass of a flat plate of length $2a_B$ in infinite fluid (Newman, 1977):

$$A_0^{plate} = \frac{1}{2}\pi\rho a_B^2. \tag{45}$$

In addition, flow separation causes in general an increase in the added mass. Further, it causes a quadratic viscous damping, strongly dependent on the KC number, defined here as $KC = U_m T/(2a_B)$, where U_m is the amplitude of the relative ambient flow velocity on the baffle (cf. Eq. (49)), and T its period. In the present cases, the resulting KC numbers in $\theta = 0°$ are less than 0.75 near the sloshing resonance, making Graham (1980)'s formulas (46) and (47) well-suited for the determination of the inertial and drag coefficients:

$$\frac{A^{plate}}{A_0^{plate}} = \alpha_0 + \alpha_1 \mathrm{KC}^{\frac{2}{3}}, \tag{46}$$

$$C_D = \alpha_2 KC^{-\frac{1}{3}}. \tag{47}$$

The empirical coefficients α_0, α_1 and α_2 are given in Table 1 for both solid and perforated flat plates in infinite fluid, as given by Mentzoni (2020) from curve-fitting with numerical simulations. The perforation ratio of the baffle τ is defined as the ratio between the perforated area divided by the total area of the baffle. $\tau = 0$ corresponds to a solid plate without perforation.

The added mass of the baffle tends to 0 when the perforation ratio increases, and the fluid velocity decreases for increasing submergence. Consequently, the shifted natural frequency σ_1' converges to σ_1 in both cases, as shown in Fig. 5. Faltinsen and Timokha (2009) compare the formula (44) to numerical and experimental results for different

Table 1
Empirical coefficients from Graham's formulas provided by Mentzoni (2020) for flat plates of perforation ratio τ in infinite fluid.

τ	α_0	α_1	α_2
0	1.000	0.216	10.1
0.15	0.281	0.271	8.72
0.30	0.017	0.181	5.48

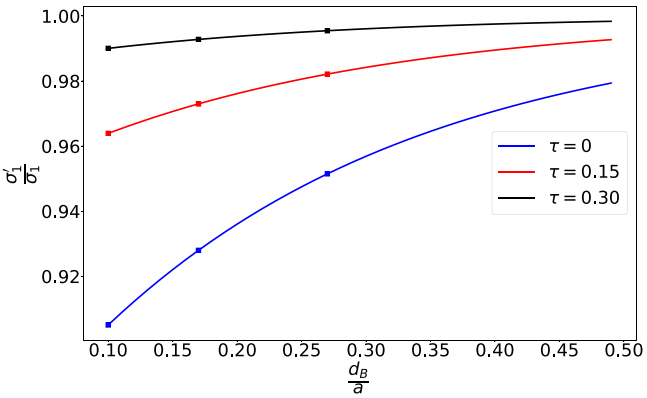

Fig. 5. Effect of baffles on the lowest natural frequency, σ_1, for solid ($\tau = 0$), and perforated baffles ($\tau = 0.15$ and $\tau = 0.30$), at different submergences d_B using the formulas (44) to (47), and the coefficients from Table 1. The equations of motions are solved for incident waves of period $\omega = \sigma_1$ and wave steepness $\epsilon = 1/60$. The rest of our work focus on three submergences, indicated here by square points. Baffles' width: $a_B/a = 0.17$.

submergences of solid baffles, with a good match for $a_B/a \leq 0.3$, and with the additional condition that the baffle should not be too close to the free surface, especially because of the apparition of local non-linearities at the free surface that are not included in the analysis, based on linear potential flow theory. Even the smallest submergence tested in our study remains however in the range showing an acceptable matching with Faltinsen and Timokha's numerical and experimental comparisons.

4.3. Estimation of the damping ratio through the energy dissipation

The local transverse, KC-dependent force of an angular section of the baffle is expressed by Morison's 2D Eq. (48) for a flat plate:

$$F_D(KC,\theta,t) = \frac{1}{2}\rho\, a_B\, C_D(KC,\theta)\, v_r(\theta,t)|v_r(\theta,t)|, \tag{48}$$

$$v_r(\theta,t) = R_1(t)\frac{\partial \varphi_1}{\partial z}\Big|_{\substack{r=a\\ z=-d_B}} + \dot{\eta}_5(t)\left[\frac{\partial \Omega}{\partial z}\Big|_{\substack{r=a\\ z=-d_B}} + a\cos(\theta)\right]. \tag{49}$$

The relative velocity v_r is given by Eq. (49) at $r = a$ and $z = -d_B$ in the tank-fixed coordinate system. Its first term corresponds to the mode $q = 1$ of the eigenfunction-expansion in Eq. (36), assuming that the first sloshing mode predominates near its resonant frequency. This approximation is expected to be adequate since the amplitudes of higher modes represent less than 3% of the first mode's amplitude in simulations with baffles for incident waves with frequencies near σ_1'. The second term is due to internal fluid motions caused by pitch.

The rate of energy dissipation during one period corresponds to the work produced by the drag force, expressed by Eq. (48), during the same period (Isaacson and Premasiri, 2001):

$$D_B = \frac{1}{T}\int_0^T \int_0^{2\pi} \frac{1}{2}\rho\, a_B C_D v_r^2 |v_r| d\theta dt. \tag{50}$$

Finally the rate of dissipation is found from:

$$\dot{E}_M = -D_B \simeq -2\sigma_1' \xi_1 E_M. \tag{51}$$

Here E_M is the mechanical energy of a standing wave oscillating at the highest natural sloshing period when the dock is not moving, with the amplitude $|\beta_1|$. It is defined as the summation of the kinetic and potential energies, $E_M = E_k + E_p$, and remains constant when there is no dissipative forces. Because the kinetic energy is maximum when the potential energy is null, and vice versa, E_M can be calculated either by E_k or E_p. The latter leads to easier calculation, and is given in the online supplement.

The damping ratio ξ_1 is obtained by Eq. (51). It is determined through an iterative scheme in the equations of motions discussed further. It reaches a local maximum at the coupled sloshing resonance, where $|\beta_1|$ is also maximum, and increases with either decreasing perforated ratio or increasing submergence of the baffle, as shown Fig. 6.

4.4. Equations of motions

The loads in this internal domain of the closed-bottom model with baffle are integrated from the dynamic pressure predicted by the potential Φ in Eq. (36):

$$F_1 = \overbrace{-\rho a^2 \pi (d+s)}^{-a_{1,1}^{\text{filled}}}\ddot{\eta}_1 + \overbrace{\rho a^2 \pi \frac{(d+s)^2}{2}}^{-a_{1,5}^{\text{filled}}}\ddot{\eta}_5 + \sum_{q=1}^{\infty} \overbrace{-\rho\left[\frac{\pi a}{k_q}\tanh\left(k_q(d+s)\right)\right]}^{g_{q,1}} \dot{R}_q(t), \tag{52}$$

$$F_5 = \overbrace{\rho a^2 \pi \frac{(d+s)^2}{2}}^{-a_{5,1}^{\text{filled}}}\ddot{\eta}_1 + \overbrace{\rho\left[-\frac{a^2(d+s)^3\pi}{3} + \sum_{j=1}^{\infty}\frac{4a^2\pi}{k_j^3(k_j^2a^2-1)}\frac{k_j(d+s)\cosh\left(k_j\frac{d+s}{2}\right) - 2\sinh\left(k_j\frac{d+s}{2}\right)}{\cosh\left(k_j\frac{d+s}{2}\right)}\right]}^{-a_{5,5}^{\text{filled}}}\ddot{\eta}_5 + \sum_{q=1}^{\infty}\underbrace{\rho\left[\frac{a\pi\left(\cosh\left(k_q(d+s)\right)-1\right)}{k_q^2\cosh\left(k_q(d+s)\right)}\right]}_{g_{q,5}}\dot{R}_q(t). \tag{53}$$

We distinguish added mass terms $a_{1,1}^{\text{filled}}$, $a_{1,5}^{\text{filled}}$, $a_{5,1}^{\text{filled}}$ and $a_{5,5}^{\text{filled}}$ caused by the internal fluid motion when the free-surface is rigid, and forces proportional to $\dot{R}_q(t)$ caused by the sloshing waves in a tank-fixed referential. These latter terms can be written as added mass and damping coefficients $a_{j,k}^{\text{slosh}}$ and $b_{j,k}^{\text{slosh}}$, $(j,k) \in \{1,5\}^2$ in the equations of motions:

$$a_{j,k}^{\text{slosh}} + \frac{i}{\omega} b_{j,k}^{\text{slosh}} = i\omega \sum_{q=1}^{\infty} g_{q,j} f_q(\omega) \tilde{P}_{q,k}(\omega) \quad (j,k) \in \{1,5\}^2 \tag{54}$$

The solution (43) of the modal equations for $\dot{R}_q(t)$ contains indeed a term in phase with the dock's acceleration, and a term in phase with the dock's velocity. If the damping ratio $\xi_1 = 0$ (absence of baffle), the potential becomes totally in phase with the dock's acceleration and the damping coefficients b^{slosh} disappear. We note that the magnitudes of the b^{slosh} coefficients are dependent on both the damping ratio, and the natural sloshing frequency. Consequently, the efficiency of the baffle depends on both its drag coefficient and its added mass.

The a^{filled} coefficients come from the first two terms of Eq. (36). They are the results of radiation problems in surge and pitch in the closed-bottom cylinder with a rigid free-surface, and without baffle.

It is possible to modify the radiation problem in Section 2.2 to replace these a^{filled} coefficients, and account for the open bottom. A rigid free-surface fixed to the dock is imposed in the domain IV, and the expansion (27) is replaced by $\phi^{IV} = \phi_h^{IV} + \phi_m^{IV}$, defined as:

$$\left.\begin{aligned}
&\phi_h^{IV}(r,z) = \psi\epsilon_0 A_0^{IV}\frac{r}{a} + \psi\sum_{p=1}^{\infty}\epsilon_p A_p^{IV}\frac{I_1(\frac{p\pi}{h}r)}{I_1(\frac{p\pi}{h}a)}\cos\left(\frac{p\pi}{h}(z+h)\right) \text{ in surge/pitch}\\
&\phi_m^{IV}(r,z) = 0 \text{ in surge}\\
&\phi_m^{IV}(r,z) = -\frac{r(z+h)^2 - \frac{r^3}{4}}{2h} \text{ in pitch}
\end{aligned}\right\} \tag{55}$$

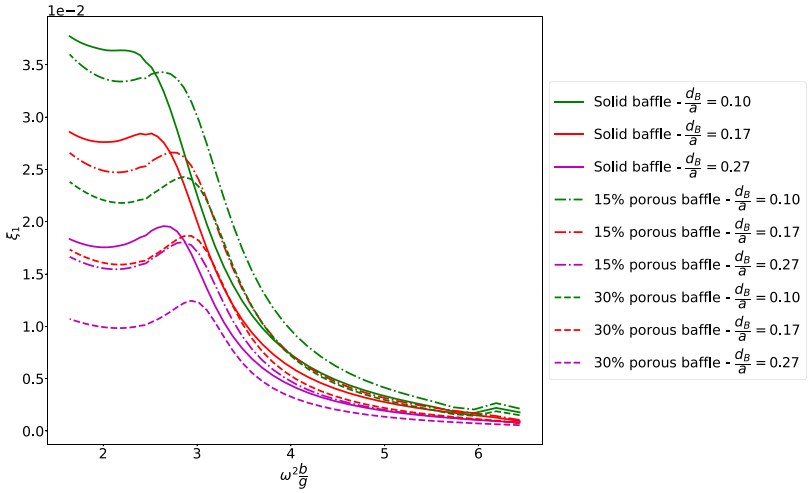

Fig. 6. Linear equivalent damping ratio due to the baffle as a function of the frequency of the incident wave as computed by our method involving Morison drag model with KC-dependent drag coefficient and strip theory and integration along the azimuthal direction (see Eqs (48) to (51)). The steepness of the incident waves is constant and equal to $\epsilon = 1/60$.

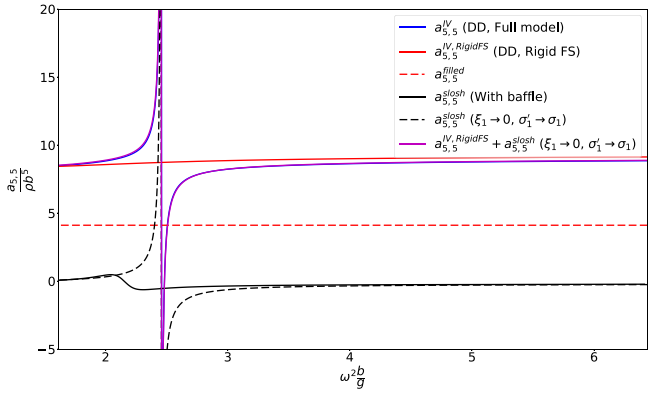

Fig. 7. Non-dimensional added moment of inertia in the internal domain IV calculated by several versions of the present DD method. $a^{IV}_{5,5}$ is obtained with the full DD model without baffle, as described in Section 2. $a^{IV,RigidFS}_{5,5}$ is obtained with the DD model that imposes a rigid free surface in the domain IV, i.e. using the expansions (55). $a^{filled}_{5,5}$ is the added moment of inertia of a cylinder with a rigid free surface and closed bottom, as defined Eq. (53), they do not account for the baffle. $a^{slosh}_{5,5}$ are the added moment of inertia of standing sloshing waves in a fixed tank, for which the effects of the baffles have been imposed through the modal equations, and defined Eq. (54). The total added moment of inertia $a^{filled}_{5,5} + a^{slosh}_{5,5}$ in the closed-bottom cylinder has been replaced by $a^{IV,RigidFS}_{5,5} + a^{slosh}_{5,5}$ to account for the open bottom. When the effects of the baffles are set to 0 ($\sigma' \to \sigma$ and $\xi_1 \to 0$), we verify that this model converges now to $a^{IV}_{5,5}$ developed in Section 2.

The improvement is illustrated by Fig. 7 for the contribution of the added moment of inertia in pitch in the domain IV. $a^{IV,RigidFS}_{5,5}$ (solid red curve), calculated from the DD method for an open-bottom dock, using the expansion (55) above, is improved by 46% compared to $a^{\text{filled}}_{5,5}$ (dash red curve) for the closed-bottom dock.

The a^{slosh} and b^{slosh} coefficients in Eq. (54), caused by standing waves in fixed tank, remain under the closed-bottom approximation, and describe entirely the effects of sloshing when an annular baffle is installed.

In addition, the moment in pitch caused by the loads acting on the baffle is expressed from Morison's 2D equation as follow:

$$F_5^M = -\int_0^{2\pi} a\left[\frac{1}{2}\rho\, a_B\, C_D(KC,\theta)\, v_r(\theta,t)|v_r(\theta,t)| + \frac{1}{4}\rho\pi a_B^2 C_M \frac{\partial v_r(\theta,t)}{\partial t}\right]\cos(\theta)d\theta, \tag{56}$$

where $C_M = A^{plate}/A_0^{plate}$ is the mass coefficient (Mentzoni, 2020), defined Eq. (46) for solid and perforated plates. Finally, the equations for the coupled surge and pitch motions are expressed in the Earth-fixed coordinate system presented Fig. 1:

$$\sum_{j=1,5}\left[-\omega^2(M_{p,j} + a_{p,j} + a^{slosh}_{p,j}) - i\omega(b_{p,j} + b^{slosh}_{p,j}) + c_{p,j}\right]\eta_j = F_p \qquad p \in \{1,5\} \tag{57}$$

where $M_{1,1} = M$ is the mass of the dock, $M_{1,5} = M_{5,1} = Mz_G$ where z_G is the centre of gravity, $M_{5,5}$ is the moment of inertia in pitch, and $c_{p,j}$ are restoring terms, from hydrostatic forces and mooring. The added mass and damping coefficients $a_{p,j}$ and $b_{p,j}$ are derived from Eq. (35) with a rigid free surface in the domain IV. F_p are the exciting loads from the diffraction problem (cf. Eq. (24)), as well as the moment (56) in pitch: $F_1 = F_1^S$ and $F_5 = F_5^S + F_5^M$. The moment F_5^M is linearised in time, but remains non-linear with regard to the motions' amplitudes $\bar{\eta}_1$ and $\bar{\eta}_5$. The Eqs. (57) are solved in the frequency domain, and the moment F_5^M calculated through an iterative process. Heave motion does not excite any sloshing mode under the closed-bottom approximation, and is uncoupled to surge and pitch. Noting furthermore that the natural frequencies of heave and piston mode are much lower than the wave frequencies of interest, we disregard η_3 hereafter.

5. Model tests

5.1. Set-up of the installation

Dedicated model tests were conducted by the authors in 2019 in the extension of the large towing tank at SINTEF OCEAN, at an imagined model scale 1:100. Two photos are provided in Fig. 8. The tank is 85 metres long from the wave maker to the parabolic beach, 10.5 metre wide, and 10 metre deep. The model was placed in the centre of the tank, fixed by four near-horizontal mooring lines and springs, each one stretched with a 65N pre-tension force. The main structure is made of aluminium, while a part of the bilge boxes was made of foam of lower density.

The internal and external radii are respectively 0.3 m, and 0.4 m. The ballast was adjusted to obtain a 0.8 m draft, while keeping the centre of gravity at 0.25 m from the bottom of the model. The moment of inertia in pitch is $I_{5,5} = 76.2$ kg m^2. The dimensions of the bilge boxes are $H_{skm} = 0.05$m high and $B_{skm} = 0.09$m wide, as presented in Fig. 9. The dimensions of the model are summarised in Table 2.

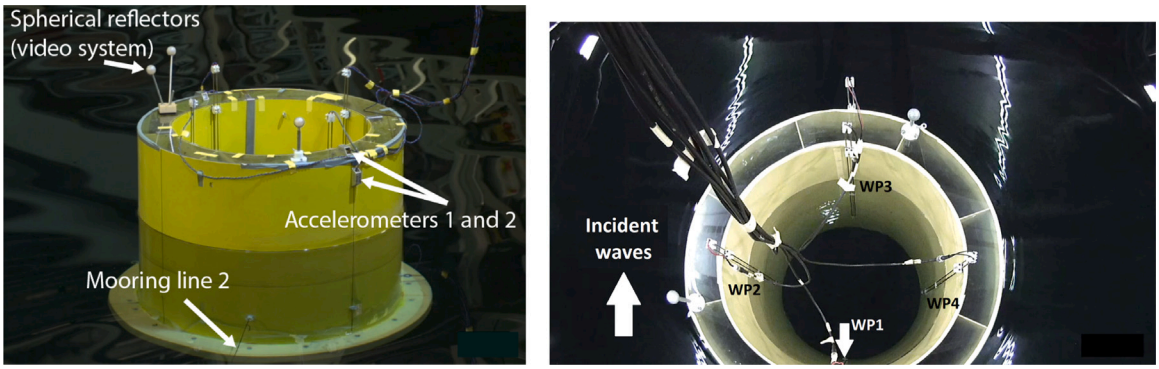

Fig. 8. Photos from the presently conducted experiments performed in the Towing Tank at SINTEF Ocean. Left: Side view. The dock is placed in the middle of the tank, fixed by four mooring lines. Rigid body motions were recorded by an optical measurement system (Oqus) with four cameras and reflectors. Right: Top view. Four wave probes fixed to the structure measure the relative free-surface elevation inside the dock.

Table 2
Dimensions of the model — Notations referring to the geometry are defined in Fig. 1.

Parameter	Unit	Value	Description
a	[m]	0.30	Inner radius
b	[m]	0.40	Outer radius
$d+s$	[m]	0.80	Draft
$H_{skm}=s$	[m]	0.05	Bilge box's height
$B_{skm}=c-b$	[m]	0.09	Bilge box's width
z_G	[m]	−0.55	Vertical location of the centre of gravity
$I_{5,5}$	[kg m^2]	76.2	Moment of inertia in pitch

Table 3
Natural periods estimated from the decay tests, in seconds, model scale. Both baffles are installed at 5 cm below the free surface.

	Dock alone	Dock+solid baffle	Dock+ Perforated baffle ($\tau=0.30$)
Surge	10.89	10.86	10.88
Heave	2.29	2.26	2.28
Pitch	2.20	2.23	2.22

Regular waves of wave period $T=0.5$s to 1.6s were tested, with a particular focus on the periods around the first sloshing resonant mode. The natural uncoupled sloshing period for a fixed-cylinder is given by (39): $T_{slosh}=2\pi/\omega_1=0.81$s. The coupled sloshing resonant peak appeared to be around $T=0.73$s, apparent as clear local maxima for surge and pitch motion, as well as the internal free surface. The wave elevation was measured at different positions by eight wave probes (denoted WP1-8). Four were fixed to the dock, and four others were fixed to the tank: two in front of the structure measuring the incident waves, and two on the side aligned with the dock. The 6 DoFs of rigid-body motion of the model were recorded using both a video positioning system and accelerometers.

5.2. Damping devices

Three types of annular baffles with perforation ratio $\tau=0$, 0.15 and 0.30 were successively installed at $d_B=0.03$, 0.05 and 0.08 m below the free-surface, cf. Fig. 10. Their width is $a_B=0.05$m, and their thickness 0.005 m. The porosity of the baffles was obtained by piercing evenly circular holes of 0.015 m diameter.

5.3. Decay tests

Decay tests were carried out with and without the baffles, giving indications on the natural periods of the different DoFs, the results are presented in Table 3. The natural period in surge was chosen to be far away from the wave periods. We note that pitch and heave resonance periods are also much higher than the sloshing natural period. They are both in the same range as the piston mode natural period, estimated from the radiation problem at $T_{piston}=2.0$s.

5.4. Time-series

The time series of WP1 to 4 were measured in a body-fixed coordinate system. The wave elevation in an Earth-fixed coordinate system was then obtained as $\zeta^{\text{Earth fixed}}=\zeta^{\text{Body fixed}}+\eta_3-x\eta_5$. Example of time series are given in Fig. 11. The signals were band-pass filtered and post-processed before reflections from the end of the tank reached back to the model, assuming deep water to calculate the group velocity of the waves: $C_g=\frac{g}{2\omega}$. The same formula was applied to remove the part of the signal from when waves reflected from the model reached WP8. Beating with the natural sloshing period was observed, especially for $T<T_{slosh}$. A special care was brought to calculate the mean amplitude of the dock's motions and WP1 to 4 over a whole number of beating periods $T_{beating}=1/|1/T_{waves}-1/T_{slosh}|$, and through a standard Fourier analysis. The transient phase before the sloshing to be fully established was about 60%–70% shorter with the presence of the baffle, thanks to the additional viscous damping.

5.5. Sources of error and uncertainty

Measurements.

The model's motions during the experiments were very small, and reaching the limit of the accuracy range that could be measured by the video positioning system. In addition, light reflections in the water were suspected to cause spurious data. Hence, accelerometers were preferred to obtain the motions of the dock.

Wave reflection and seiching

Longitudinal standing waves (seiching) were sometimes observed in the time series for the longest waves. However, their period $T_{seiching}=2L/\sqrt{gh}=17.16$s was filtered efficiently. Reflection from the lateral walls was also an issue. The waves' amplitude measured by WP6 and WP7 at the walls could differ up to 30% compared to WP8 in front of the model, especially for short waves.

Symmetry

The model was not perfectly symmetric, due to several factors: the compartmentation of the ballasts, a variation of few millimetres in the internal and external radii from the fabrication, non-identical pre-tension in each mooring line. This may explain partially the observation of very small roll and sway motions during the tests.

Repetition tests

Selected regular wave conditions were repeated to investigate the importance of random error. The average standard deviation was in the range of 1.5%–3% for the motions of the dock, and 5%–10% for the

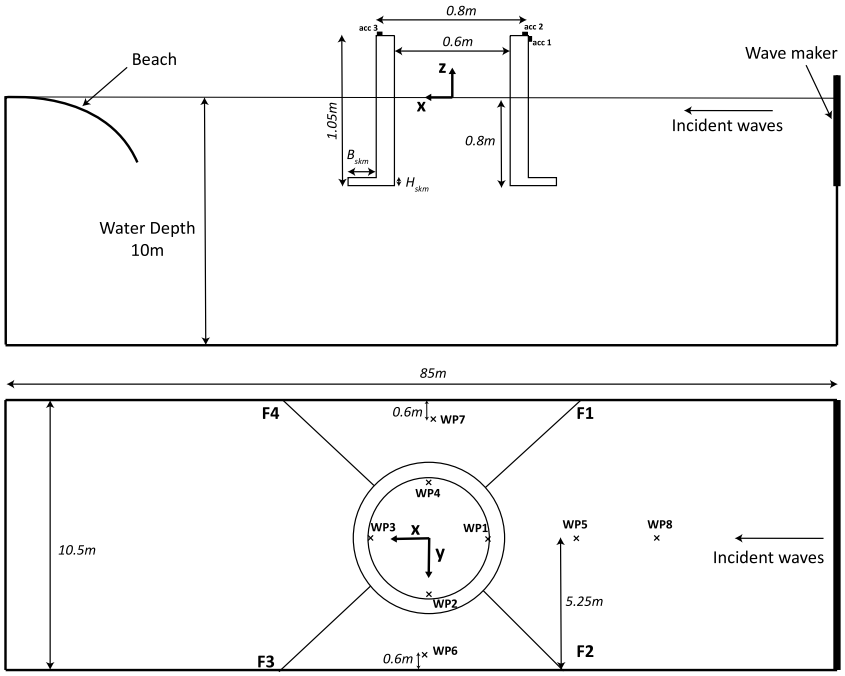

Fig. 9. Side and bird's-eye views of the experimental set-up. The wave probes WP1 to WP4 are fixed inside the model, and WP5 to WP8 are fixed to the tank. Two vertical and one horizontal accelerometers (acc) are fixed on the top of the model. Four mooring lines with four springs are stretched symmetrically with a pretencion of 65N, and an angle of 11° to the horizontal.

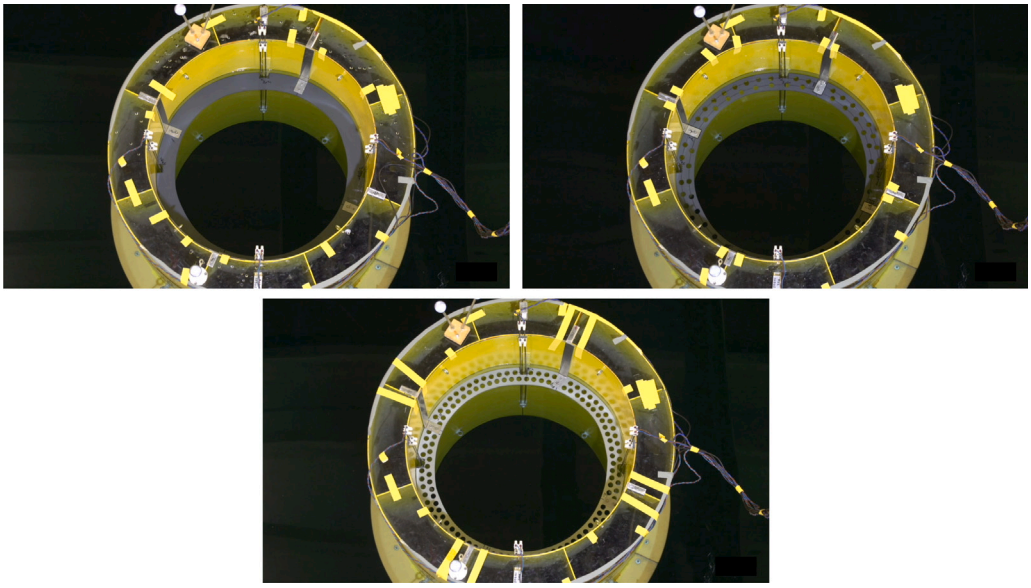

Fig. 10. Photos showing the three different baffles that were tested in November 2019. Top left: solid baffle. Top right: perforated baffle ($\tau = 0.15$). Bottom: perforated baffle ($\tau = 0.30$).

free-surface elevation, with the largest error near the coupled resonant peak. The shortest incident regular waves that were tested had among the highest frequencies that could be generated by the wave-maker. During two identical repetition tests, the measured wave frequency could differ by 1%–2%.

6. Results

We first present results from the case without baffles, and next with baffles.

6.1. RAOs for the dock without baffle

The response amplitude operator (RAO) of the dock's surge and pitch motions, and of the wave elevation inside the dock, located at WP1 and given in the Earth-fixed coordinate system, are presented in Fig. 12 for the case without baffle. Results from the linear DD method developed in Section 2 are compared to experimental results for three wave steepnesses, $\epsilon = 2A/\lambda = 1/60$, $1/45$ and $1/30$, where A is the wave amplitude and λ the wave length of the incident waves. At the non-dimensional natural sloshing frequency $\omega^2 b/g = 2.45$, small dock motions cause large sloshing waves, increasing significantly the added mass of the system as discussed Section 3. Consequently, both the RAOs

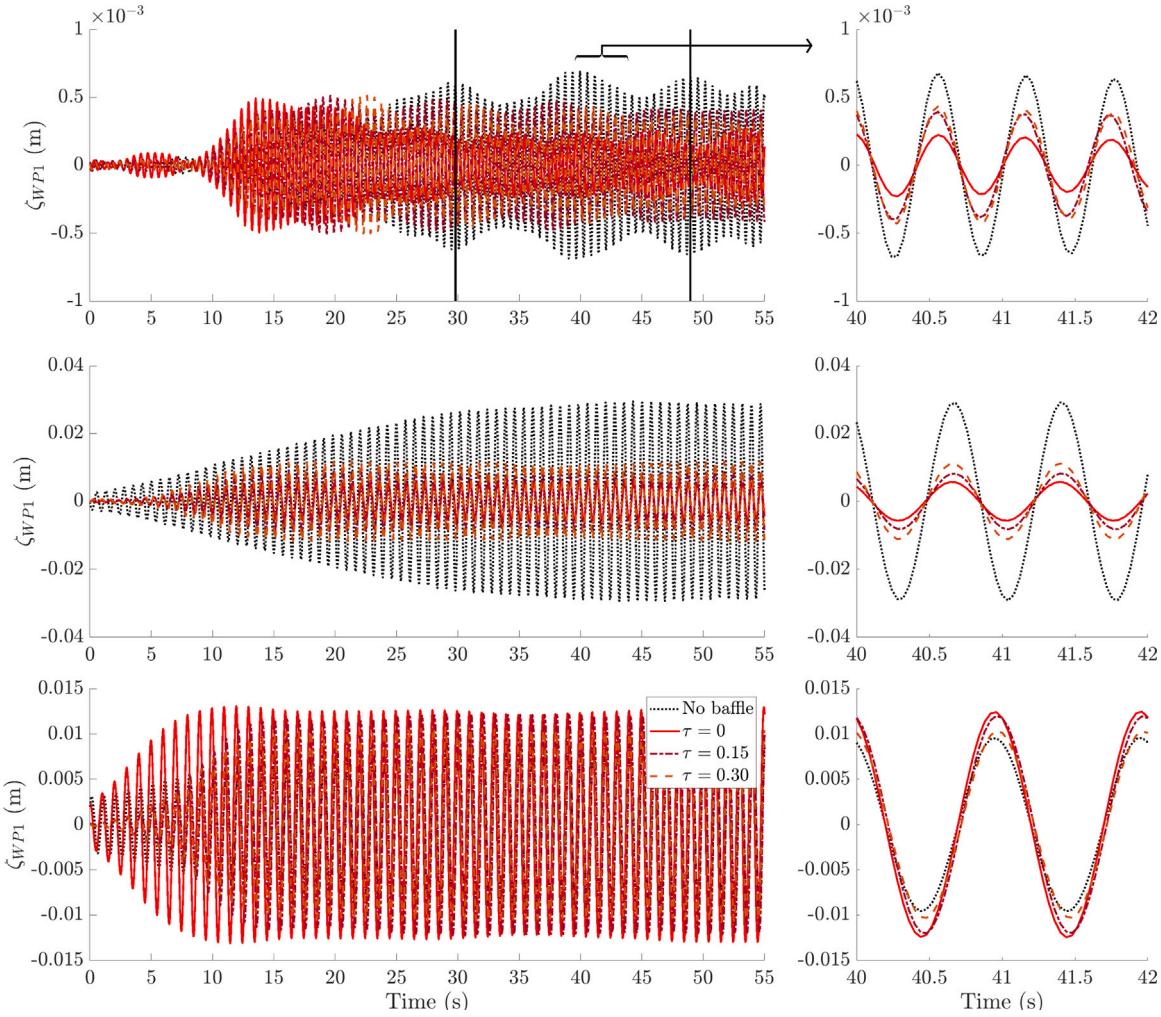

Fig. 11. Examples of experimental time series of the wave elevation in an Earth-fixed reference frame. Cases with baffle submergence $d_B/a = 0.17$. Top: $T = 0.60s$, the vertical bars delimit two beating periods . Middle: $T = 0.74s$. Bottom: $T = 1s$.

in surge and pitch are converging to nearly 0 at this frequency. The maximum amplitude of both the internal free-surface elevation and motions are observed at the coupled resonant frequency $\omega^2 b/g = 3.0$, in particular our model gives $(\zeta_{WP1}/A)_{max} = 3.62$. Inaccuracies when modelling the inertial and restoring coefficients of the floating dock similar to the model tests are suspected to cause a slight shift between analytical and experimental results.

The variations due to the different wave steepnesses are in overall quite small. Despite some scattering near the resonant peak, the general trend shows that the peak amplitude tends to decrease for increasing incident wave steepness. The most notable difference is observed in surge near $\omega^2 b/g = 3.0$, the response for $\epsilon = 1/60$ being about 12.4% higher than for $\epsilon = 1/30$, and is suspected to be caused by viscous damping in surge. In order to account for this viscous dissipation, a quadratic drag force in surge is introduced in the equations of motions:

$$F_D = -\frac{1}{2}\rho C_D 2b(d+s)\dot{\eta}_1|\dot{\eta}_1|. \tag{58}$$

The force is linearised, such that the energy dissipated over one period of oscillation is identical:

$$F_D \simeq i\omega^2 \frac{8}{3\pi} C_D b(d+s)\bar{\eta}_1|\bar{\eta}_1|e^{-i\omega t}. \tag{59}$$

Because of the low KC numbers (KC≤ 0.7), flow separation is most likely to occur at the bottom of the body. The results presented in Fig. 12 are obtained for $C_D = 3$, and show a reduction of the resonant peak's amplitude between 8.8% for $\epsilon = 1/60$ and 15.8% for $\epsilon = 1/30$. Similar rates are observed for ζ_{WP1}, suggesting that viscous forces on the dock could also be used as a mean to damp sloshing waves.

6.2. RAOs for the dock with solid and porous baffles

We next investigate the effectiveness of the baffles. The surge motion of the dock is given in Fig. 13, and WP1 in Fig. 14, for three baffle submergences d_B/a. The presence of the baffle reduces significantly the amplitude of the surge motions and of the internal free-surface elevation near resonance. The best baffle efficiency is obtained experimentally for the solid baffle at the lowest submergence, with a maximum sloshing amplitude as low as $(\zeta_{WP1}/A)_{max} = 1.58$, as predicted by our numerical method for the lowest baffle submergence $d_B/a = 0.27$. Increasing perforated ratio reduces the viscous damping ξ_1, and the resonant natural frequency converges to the case without baffles (see Fig. 14, $\tau = 0.3$). We mention that similar damping as for surge was obtained for the pitch motion (not shown), with a maximum decrease of the resonant peak amplitude in pitch of 27% from the case without baffle, as obtained analytically for the solid baffled at $d_B/a = 0.17$.

Because the total damping also depends on the natural frequency σ_1, the analytical method predicts almost the same reduction of the RAOs' amplitudes in Figs. 13 and 14 for $\tau = 0.15$ as for the solid baffle.

The analytical method succeeds to catch the shift of natural frequency, and presents a quite good agreement with the experimental

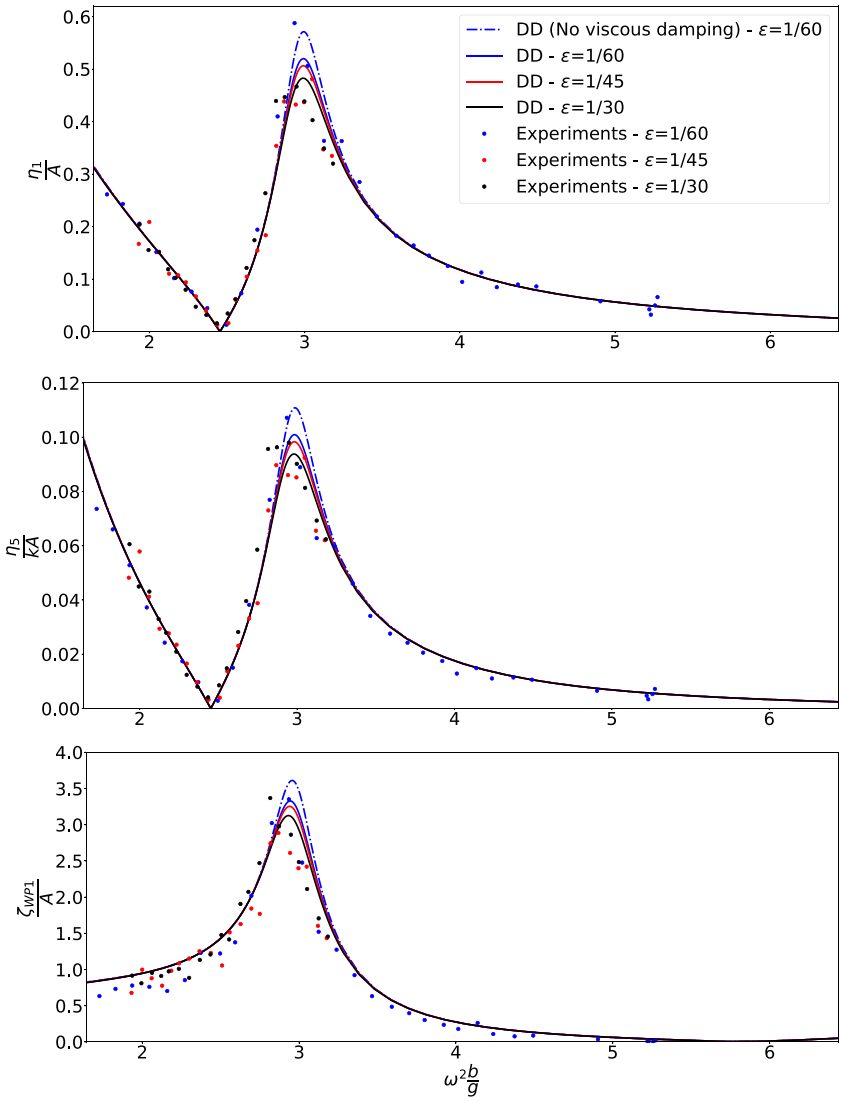

Fig. 12. RAO of the dock's surge (top) and pitch (middle), and RAO of the wave elevation inside the dock at WP1 (bottom), calculated from the DD approach and compared to experimental results for three different wave steepnesses, for the case without baffles. The dash curves show the motions calculated analytically without any viscous damping, while a drag force (cf. (58)) is added in the equation of surge for the solid curves.

results for the highest submergence $d_B/a = 0.27$. However, the damping at lower submergence is under-predicated for the solid baffle, resulting in higher predicted responses than found in the model tests. This means that our model is conservative. The increase of the damping coefficient for flat plates at low submergence has been pointed out in studies as Song and Faltinsen (2013) and Vottestad (2020) through experimental and numerical works. They also show that the added mass coefficient of the plates is expected to be lower at low d_B/a than in infinite fluid for low KC numbers. Local non-linear behaviour of the free-surface flow was observed from videos of the experiments for $d_B/a = 0.10$, which could also explain somewhat more scatter in the experimental RAOs for the two lower submergences, and especially the wide span of results obtained for the two repetition tests with a solid baffle.

In order to investigate the effect of free-surface interaction, the α_i coefficients in Eqs (46) and (47) can be tuned to match the experimental results. Examples are provided in Figs. 13 and 14 for the solid baffle, represented by the dashed curves denoted DD2 in the legend. Similar variations as found in the literature (Vottestad, 2020) of the added mass and damping coefficients of a flat plate oscillating from deep to lower submergences are applied. The coefficients from Table 1 are here replaced (dash lines) by $\alpha_1 = 0.21$ and $\alpha_2 = 18.18$ for $d_B/a = 0.10$, and $\alpha_1 = 0.19$ and $\alpha_2 = 19.70$ for $d_B/a = 0.17$. This means that the drag coefficient is almost doubled. The results indicate that improvements can be made to our model by studying forced motion of solid and perforated 2D plates near a free surface, or as a first estimation, near a solid wall.

The phases of η_1 and ζ_{WP1} are given in Fig. 15 without and with solid baffle. The sudden shift of π in the surge's phase (also observed in pitch) at the natural sloshing frequency results from the change of sign in Eq. (43) when $\xi_1 = 0$. The surge acceleration becomes then in opposition of phase with the wave elevation, and the surge motion in phase, for higher frequencies. Some of the measured signals presented unexpected phases, which could not be explained by physical phenomena that would have been visible from the videos. However, in general the main trends remain clearly distinguishable, and tend to be consistent with the analytical approach. A main observation is that the phase shift is significantly less pronounced when baffles are included.

7. Comments

The method is restricted to circular shaped dock. Further, the damping model is restricted to draft-to-diameter ratios that are in the order of unity or more. Therefore, the hybrid analytical model that includes

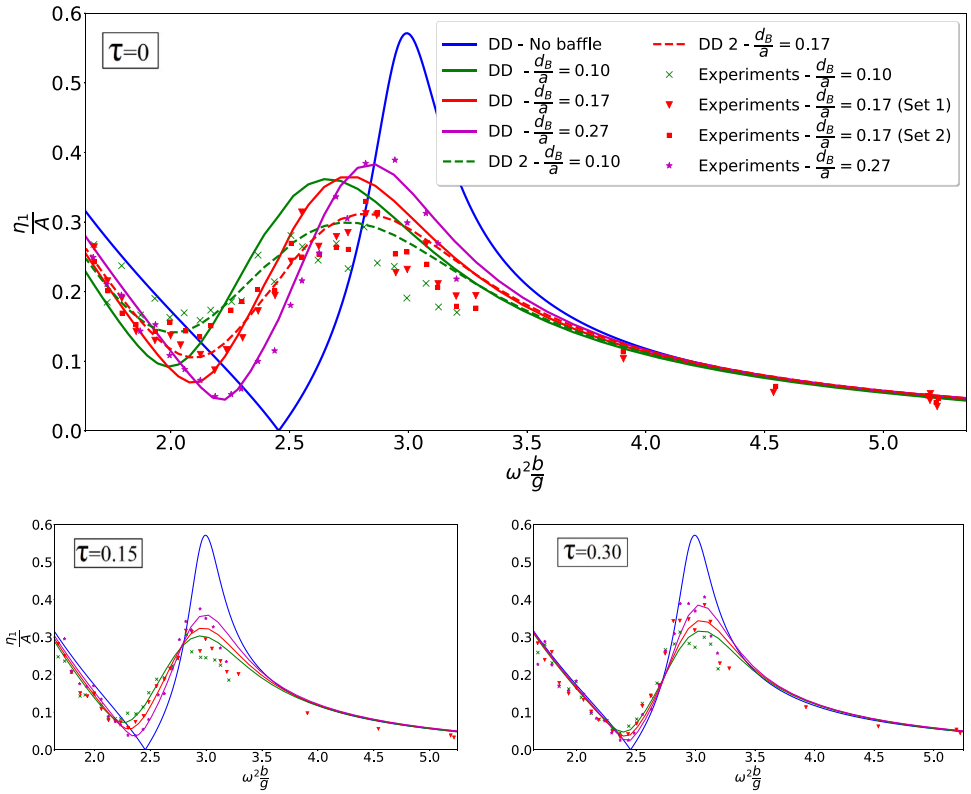

Fig. 13. RAOs in surge for three different submergences d_B/a of the baffles. Top: solid baffle. The dashed lines (DD 2) are obtained for lower, respectively higher, added mass and damping coefficients of the baffle, in order to account for free-surface interaction. Bottom left: $\tau = 0.15$. Bottom right: $\tau = 0.30$.

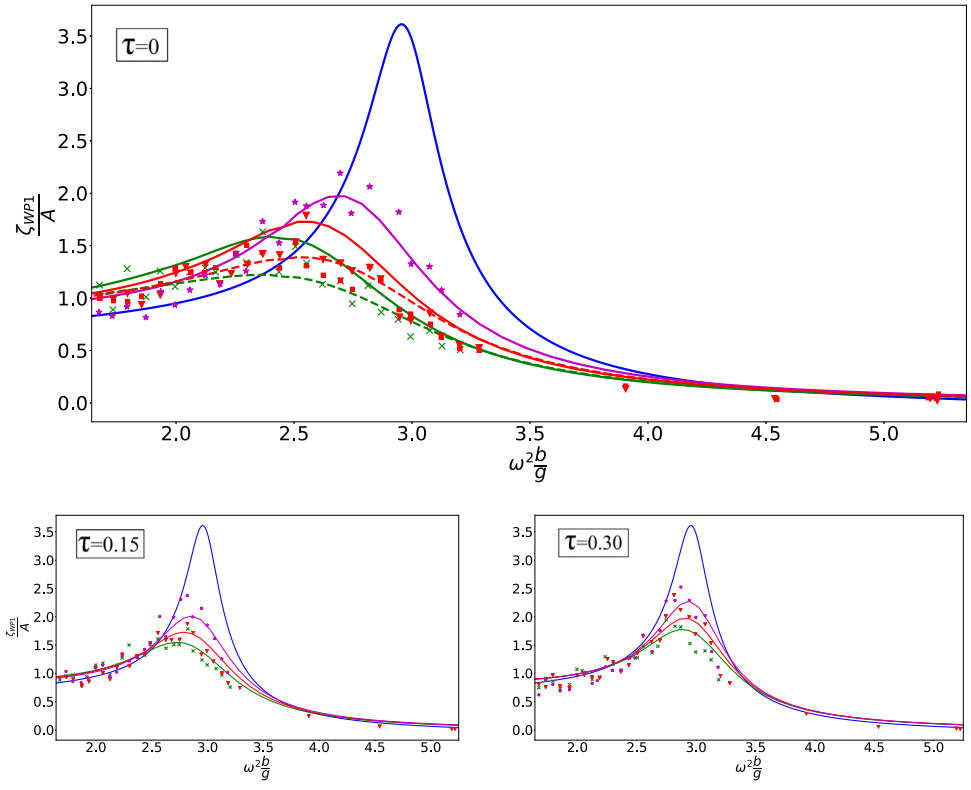

Fig. 14. Earth-fixed RAOs of the free-surface elevation at WP1 inside the dock for three different submergences d_B/a of the baffles. Top: solid baffle. Bottom left: $\tau = 0.15$. Bottom right: $\tau = 0.30$. Same legend as Fig. 13.

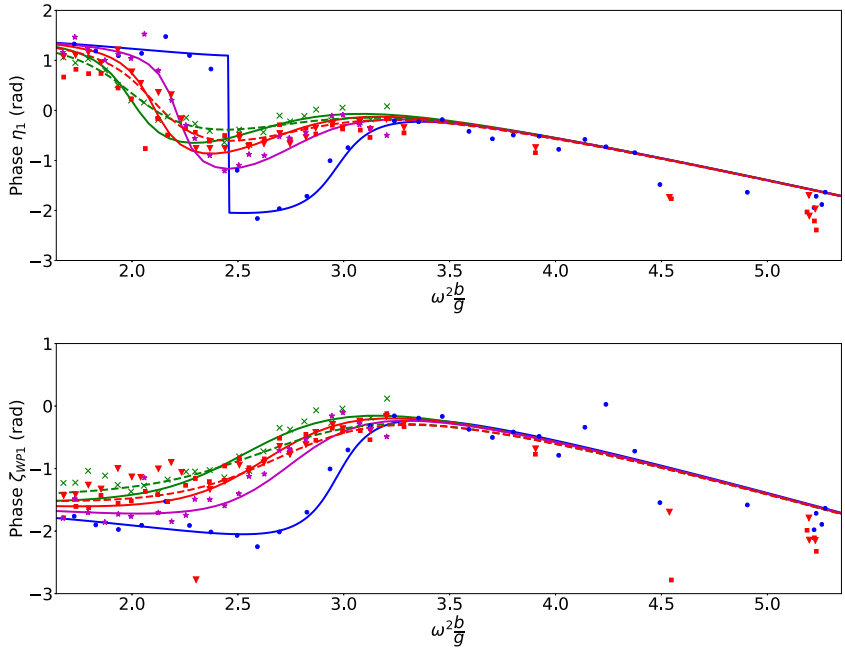

Fig. 15. Phases of surge motion (top) and WP1 (bottom) relative to the incident wave at the origin of the Earth-fixed coordinate system for the dock with a solid baffle. Same legend as Fig. 13.

the baffles is not very general. However, compared to, for instance, a panel code, the method allows for extensive parameter studies of the geometry and the mass, as well as the size, the position, and perforated ratio of the baffle, without the work of re-meshing. Multiple baffles can readily be modelled by using added mass and damping coefficients for two or more parallel plates (cf. Mentzoni (2020)). Other damping mechanics, like for instance moving walls or pumps along the internal walls can also be modelled with a limited effort.

The method is coded in Python, the CPU time is of few seconds per wave frequency on an Intel i7 desktop, and few minutes for one run with 80 frequencies.

8. Conclusion

A floating dock for installing deep-draft offshore floating wind turbines was studied. Wave frequencies in the vicinity of the first sloshing mode was considered through both analytical and experimental works.

A potential flow code based on a domain decomposition approach was first developed to solve linear diffraction and radiation problems, taking advantage of the symmetry of revolution. Added mass and damping coefficients, as well as exciting forces and moments were compared to results obtained from the panel code WAMIT with good agreements.

Solid and perforated baffles were introduced inside the structure to damp the sloshing and corresponding surge and pitch motions. The analytical method was extended using known theories for annular baffles in closed-bottom cylinders (cf. Faltinsen and Timokha (2009)). The best efficiency was achieved by the solid baffles, for which comparisons with the experimental results showed good agreement when the baffles were far from the free surface ($d_B/a = 0.27$), but under-predicted the damping due to the baffles for lower submergences, most probably due to interactions with the free-surface. Baffles with a perforation ratio $\tau = 0.15$ were shown to be almost as efficient as solid baffles in reducing the amplitudes of the free-surface elevation and dock's motions, and could provide lighter and cheaper alternatives.

Further work will include the free-floating SPAR of a FOWT inside the dock, in the light of limiting criteria for wind turbine assembly in order to investigate the feasibility of the such a floating dock to be an installation vessel for FOWT farms.

CRediT authorship contribution statement

Maël Moreau: Conceptualization, Methodology, Formal analysis, Investigation, Writing – original draft. **Trygve Kristiansen:** Conceptualization, Methodology, Writing – review & editing, Supervision, Funding acquisition. **Babak Ommani:** Investigation, Writing – review & editing, Supervision. **Bernard Molin:** Formal analysis, Writing – review & editing.

Declaration of competing interest

The authors declare that they have no known competing financial interests or personal relationships that could have appeared to influence the work reported in this paper.

Acknowledgements

This work has been conducted at the Norwegian University of Science and Technology (NTNU), partially supported by the Centre for Research-based Innovation of Marine Operations (SFI MOVE) within the Research Council of Norway.

Funding

This work has been supported by both the Norwegian University of Science and Technology (NTNU), Norway, and the Centre for Research-based Innovation of Marine Operations (SFI MOVE) within the Research Council of Norway.

Appendix A. Supplementary data

Supplementary material related to this article can be found online at https://doi.org/10.1016/j.apor.2021.102934.

References

Abramson, H.N., 1966. The Dynamic Behavior of Liquids in Moving Containers, with Applications to Space Vehicle Technology. Scientific and Technical Information Division, National Aeronautics and Space Administration; for sale by Supt. of Docs., U. S. Govt. Print. Off..

Faltinsen, O.M., Timokha, A., 2009. Sloshing, first edition Cambridge University Press.

Garrett, C., 1971. Wave forces on a circular dock. J. Fluid Mech. 46, 129–139.

Gavrilyuk, I., Lukovsky, I., Trotsenko, Y., Timokha, A., 2006. Sloshing in a vertical circular cylindrical tank with an annular baffle. Part 1. Linear fundamental solutions. J. Eng. Math. 54.

Graham, J., 1980. The forces on sharp-edged cylinders in oscillatory flow at low keulegan-carpenter numbers. J. Fluid Mech. 97, 331–346.

Isaacson, M., Premasiri, S., 2001. Hydrodynamic damping due to baffles in a rectangular tank. Can. J. Civil Eng. 28, 608–616.

Jiang, Z., Yttervik, R., Gao, Z., Sandvik, P., 2020. Design, modelling, and analysis of a large floating dock for spar floating wind turbine installation. Mar. Struct. 72.

Lee, C., Newman, J., 2006. Wamit user manual, versions 6.3, 6.3pc, 6.3s, 6.3s-PC.

Mavrakos, S., 1985. Wave loads on a stationary floating bottomless cylindrical body with finite wall thickness. Appl. Ocean Res. 7, 213–224.

Mavrakos, S., 1988. Added mass and damping of a vertical cylinder in finite-depth waters. Ocean Eng. 15, 213–229.

Mentzoni, F., 2020. Hydrodynamic Loads on Complex Structures in the Wave Zone (Doctoral thesis).

Miles, J., Gilbert, F., 1968. Scattering of gravity waves by a circular dock. J. Fluid Mech. 34, 783–793.

Molin, B., 2001. On the piston and sloshing modes in moonpools. J. Fluid Mech. 430, 27–50.

Morison, J.R., O Brien, M.P., Johnson, J.W., Schaaf, S.A., 1950. The force exerted by surface waves on piles. J. Pet. Technol. 2, 149—154.

Newman, J.N., 1977. Marine Hydrodynamics, first ed. The MIT Press.

Sabuncu, T., Calisal, S., 1981. Hydrodynamic coefficients for vertical circular cylinder at finite depth. Ocean Eng. 8, 25–63.

Sommerfeld, A., 1948. Vorlesungen über theoretische physik. Leipzig Akd. Verlagsgesellschaft 69.

Song, A., Faltinsen, O.M., 2013. An experimental and numerical study of heave added mass and damping of horizontally submerged and perforated rectangular plates. J. Fluids Struct. 39, 87–101.

Vottestad, K., 2020. Experimental Study of Hydrodynamic Loads on Ventilated Plates Near the Free Surface (Master thesis).

Wang, W., Peng, Y., Zhou, Y., Zhang, Q., 2016. Liquid sloshing in partly-filled laterally-excited cylindrical tanks equipped with multi baffles. Appl. Ocean Res. 59, 543–563.

Yeung, R., 1980. Added mass and damping of a vertical cylinder in finite-depth waters. Appl. Ocean Res. 3, 63–80.